

A Multi-scale CNN-CRF Framework for Environmental Microorganism Image Segmentation

Jinghua Zhang, Chen Li, Frank Kulwa, Xin Zhao, Changhao Sun, Zihan Li, Tao Jiang, and Hong Li

Abstract—In order to assist researchers to identify *Environmental Microorganisms* (EMs) effectively, a *Multi-scale CNN-CRF* (MSCC) framework for the EM image segmentation is proposed in this paper. There are two parts in this framework: The first is a novel pixel-level segmentation approach, using a newly introduced *Convolutional Neural Network* (CNN), namely “mU-Net-B3”, with a dense *Conditional Random Field* (CRF) post-processing. The second is a VGG-16 based patch-level segmentation method with a novel “buffer” strategy, which further improves the segmentation quality of the details of the EMs. In the experiment, compared with the state-of-the-art methods on 420 EM images, the proposed MSCC method reduces the memory requirement from 355 MB to 103 MB, improves the overall evaluation indexes (Dice, Jaccard, Recall, Accuracy) from 85.24%, 77.42%, 82.27% and 96.76% to 87.13%, 79.74%, 87.12% and 96.91% respectively, and reduces the volume overlap error from 22.58% to 20.26%. Therefore, the MSCC method shows a big potential in the EM segmentation field.

Index Terms—Environmental Microorganisms, Image Segmentation, Multi-scale Analysis, Deep Convolutional Neural Networks, Conditional Random Fields.

I. INTRODUCTION

In many countries, environmental pollution is an extremely serious problem. Therefore, many methods to deal with environmental pollution are constantly putting forward. The methods of eliminating environmental pollution can be divided into three major categories: chemical, physical and biological. By contrast, the biological method is more harmless and well efficient [1]. *Environmental Microorganisms* (EMs) are microscopic organisms living in the environments which are natural decomposers and indicators [2]. For example, *Actinophrys* can digest the organic waste in sludge and increase the quality of fresh water, whereas *Rotifera* can decompose rubbish in water and reduce the level of eutrophication. Therefore, the research of EMs plays a significant role in the management of pollution [3]. The identification of EMs is the basic step for related researches.

Generally, there are four traditional types of EM identification strategies. The first one is the chemical method, which

is highly accurate but often results in secondary pollution of chemical reagent [4]. The second strategy is the physical method. This method also has high accuracy, but it requires the expensive equipment [4]. The third is molecular biological method which distinguishes EMs by sequence analysis of genome [5]. This strategy needs expensive equipments, plenty of time and professional researchers. The fourth strategy is morphological observation which needs an experienced operator to observe EMs under a microscope and give the EM identities by their shape characteristics [1]. Hence, these traditional methods have their respective disadvantages in practical work.

The morphological method has the lowest cost of the above methods, but requires a large amount of labour. Considering that deep learning achieves good performance in many fields of imaging processing, it can be used to make up the drawbacks of the traditional morphological method. Thus, we propose a full-automatic system for the EM image segmentation task which can obtain the EM shape characteristics to assist researchers to detect and identify EMs effectively. The proposed system has two parts: The first part is a novel deep *Convolutional Neural Network* (CNN), namely “mU-Net-B3”, with a *Conditional Random Field* (CRF) based pixel-level segmentation approach; the second part is a VGG-16 network [6] based patch-level segmentation method. By the pixel-level part, high quality segmentation results are obtained on most EM images, but losing effectiveness on some details with under-segmentation problems in some images. Therefore, we propose the patch-level part to assist the system to obtain more details of EMs. Hence, our *Multi-scale CNN-CRF* (MSCC) segmentation system is able to solve the EM image segmentation effectively.

In the pixel-level part, mU-Net-B3 with denseCRF is used as the core step for the segmentation task, where mU-Net-B3 is an improved U-Net. Compared with U-Net, it effectively improves the performance of segmentation results and reduces the memory requirement. Because denseCRF [7] can obtain the global information between pixels in an image, it is used as the post-processing after mU-Net-B3, which further improves the performance of the segmentation results. In the patch-level part, the segmentation task is actually a binary classification task. Because of the outstanding classification ability of VGG-16 in ImageNet [6] and the significant performance of transfer learning with limited training data set, we use the limited EM training data to fine-tune the VGG-16 model pre-trained by ImageNet, which provide hundreds of object categories and millions of images [6], in our patch-level part. This approach effectively generates good classification results, from which

J. Zhang, C. Li, F. Kulwa, C. Sun, Z. Li, and H. Li are with Microscopic Image and Medical Image Analysis Group, MBIE College, Northeastern University, Shenyang 110169, PR China.

X. Zhao is with Environmental Engineering Department, Northeastern University, Shenyang 110169, PR China.

T. Jiang is with Control Engineering College, Chengdu University of Information Technology, Chengdu 610103, China.

Corresponding author: C. Li. E-mail: lichen201096@hotmail.com

This work is supported by the National Natural Science Foundation of China (No. 61806047), the Fundamental Research Funds for the Central Universities (No. N171903004, N180719020, N2019003) and the China Scholarship Council (No. 2017GXZ026396).

we reconstruct the patch-level segmentation results. The EM segmentation framework is shown in Fig. 1.

In Fig. 1, (a) denotes the ‘Training Images’: The training set contains 21 categories of EM images and their corresponding ground truth (GT) images. We unify the image size to 256×256 pixels. Considering the color information is inefficient in EM segmentation [8], these images are converted into grayscale images; (b) shows the ‘Patch-level Training’: Images and their corresponding GT images are meshed into patches (8×8 pixels). Then the data augmentation operation is used to balance patch data. After that, the balanced data are used to fine-tune the pre-trained VGG-16 to obtain the classification model; (c) is the ‘Pixel-level Training’: Data augmentation is applied to make up the lack of data. Then, the data is fed to the mU-Net-B3 to obtain the segmentation model; (d) is ‘Testing Images’: The test set only has original images. We respectively convert them into grayscale images and patches for pixel-level and patch-level tests; (e) denotes the ‘Pixel-level Post-processing’: The denseCRF is used to further improve the pixel-level segmentation results; (f) shows ‘Patch-level Post-processing’: The predicted labels of patches are used to reconstruct the patch-level segmentation results. For further optimization, the denseCRF results are used to build up the buffers to help the patch-level results to denoise. (g) is the ‘Final Results’: The denseCRF results and buffer results are combined and plotted by different colors on the original images.

The main contributions in this paper are as follows:

- We propose a novel automatic approach which segments EM images from pixel-level and patch-level to assist EM analysis work.
- We propose three different strategies to optimize the original U-Net from the perspective of receptive field, which well improve the segmentation performance.
- The proposed U-Net-B3 not only improves the segmentation performance but also reduces the memory requirement to less than a third of that of U-Net.

The structure of this paper is as follows: Sec. II is the related work about existing EM segmentation methods. Sec. III gives detailed description on our proposed method. Sec. IV introduces experiment settings, evaluation methods and results. Sec. V closes this paper with a brief conclusion.

II. RELATED WORK

A. Existing Microorganism Segmentation Methods

In this section, related works about microorganism image segmentation techniques are briefly summarized, including classical and machine learning based methods. For more details, please refer to our previous survey in [9].

1) *Classical Methods*: Classical methods include three sub-categories, which are threshold based methods, edge based methods and region based methods. Threshold based methods: The related work [10] shows a comparison between threshold based segmentation methods for biofilms. The last result shows iterative selection method is superior; In [11], different algorithms which are based on Otsu thresholding are applied for segmentation of floc and filaments to enhance

monitoring of activated sludge in waste water treatment plants. Edge based methods: A segmentation and classification work is introduced to identify individual microorganism from a group of overlapping (touching) bacteria in [12]. Canny is used as the basic step of the segmentation part in [12]; In [13], in order to be able to segment large size images of zooplanktons, a segmentation (based on Active Contour) and pre-classification algorithm is used where after acquisition of images. Region based methods: In [14], the segmentation is performed on gray level images using marker controlled watershed method; In [15], after converting the color mode and using morphological operations to denoise, seeded region-growing watershed algorithm is applied for segmentation.

2) *Machine Learning Methods*: Machine learning methods usually have two categories: unsupervised and supervised methods. Unsupervised methods: [16] makes an evaluation about clustering and threshold segmentation techniques on tissue images containing TB Bacilli. The final result shows that k -means clustering ($k = 3$) is outstanding; In [17], a comparison between condition random fields and region based segmentation methods is presented. The final result shows that these two kinds of methods for microorganism segmentation have the average recognition rate above 80%. Supervised Methods: In [18], a segmentation system is designed to monitor the algae in water bodies. Its main thought is image enhancement (sharpening) applied first by using Retinex filtering technique, then segmentation is done by using support vector machine; In [19], Rift Valley Virus is segmentation subject. Because of the insufficient data set, data augmentation is used to assist U-Net, which is used for segmentation.

B. Machine Learning Methods

In this section, the methods related to our work are introduced, including U-Net [20], Inception [21], denseCRF [7] and VGG-16 [6].

1) *U-Net*: U-Net is a convolutional neural network, which is initially used to perform the task of medical image segmentation. The architecture of U-Net is symmetrical. It consists of a contracting path and an expansive path [20]. There are two important contributions of U-Net. The first is the strong using of data augmentation to solve the problem of insufficient training data. The second is its end-to-end structure, which can help the network to retrieve the information from the shallow layers. With the outstanding performance, U-Net is widely used in the task of semantic segmentation. The network structure of U-net is shown in Fig. 2.

2) *Inception*: The original Inception, which uses filters of different sizes (1×1 , 3×3 , 5×5), is proposed in GoogleNet [22]. Because of the use of these filters, Inception has the capacity to adapt objects that have various sizes in images. However, there are also some disadvantages with the different filters used. For instance, the increasing of parameters, overfitting and vanishing gradient. To reduce the negative effects, Inception V2 gives a novel method, which is combining two 3×3 convolution filters to replace one 5×5 convolution filter [21]. For further optimization, Inception-V3 proposes a better approach, which uses a sequence of

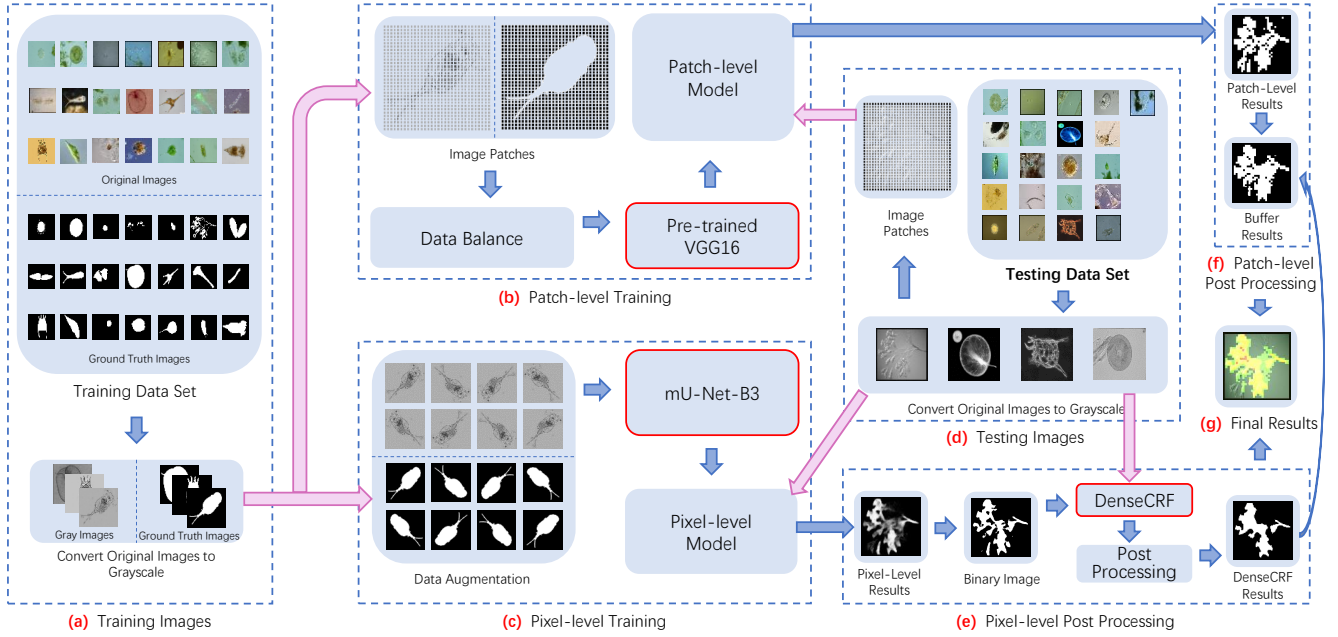


Fig. 1. An overview of our MSCC EM segmentation framework.

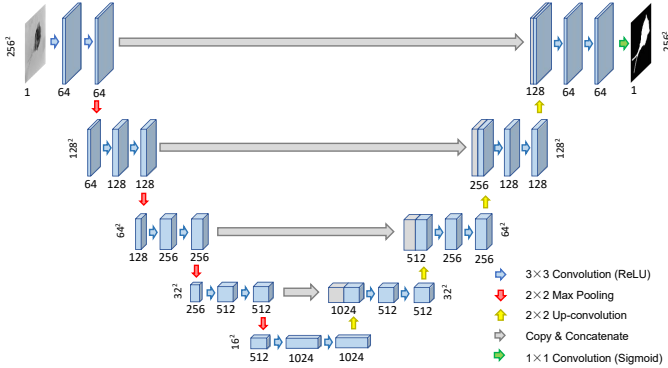
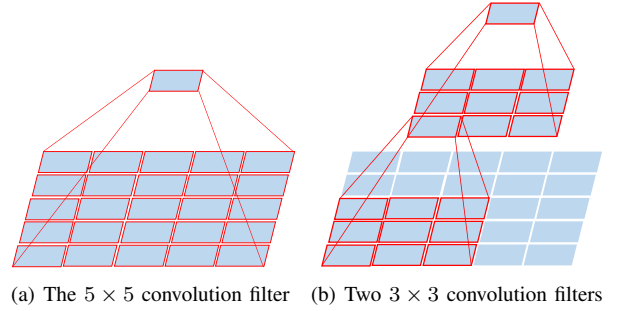


Fig. 2. The network structure of U-Net.

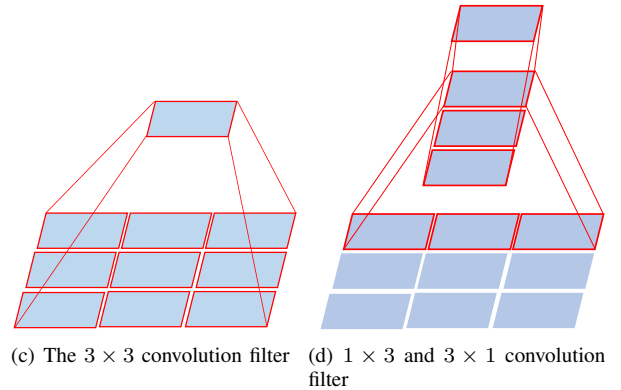
$1 \times N$ convolution filter and $N \times 1$ convolution filter to replace $N \times N$ convolution filter [21]. Fig. 3 also shows the 3×3 convolution filter replaced by 1×3 and 3×1 convolution filters. This strategy reduces more parameter count. Furthermore, with more convolution filters with ReLU used, the expressiveness is improved.

3) *DenseCRF*: Although CNNs can perform well on pixel-level segmentation, there are still some details that are not perfect enough. The main reason is it's difficult to consider the spatial relationships between different pixels in the process of pixel-level segmentation by CNNs. However, [23] shows using denseCRF as post-processing after CNNs can capture the spatial relationships. It can improve the segmentation results. In [7], the energy function of denseCRF model is the sum of unary potential and pairwise potential, which is shown in Eq. 1.

$$E(\mathbf{x}) = \sum_i U(x_i) + \sum_{i,j} P(x_i, x_j) \quad (1)$$



(a) The 5×5 convolution filter (b) Two 3×3 convolution filters



(c) The 3×3 convolution filter (d) 1×3 and 3×1 convolution filter

Fig. 3. The strategies used by Inception-V2 and Inception-V3 to replace the big filter.

In Eq. 1, \mathbf{x} is the label assignment of pixel. $U(x_i)$ represents the unary potential, which measures the inverse likelihood of the pixel i taking the label x_i , and $P(x_i, x_j)$ means the pairwise potential, which measures the cost of assigning labels x_i, x_j to pixels i, j simultaneously [24]. We use the Eq. 2 as unary potential, where $L(x_i)$ is the label

assignment probability at pixel i .

$$U(x_i) = -\log L(x_i) \quad (2)$$

The pairwise potential is defined as Eq. 3, where $\phi(x_i, x_j)$ is a penalty term on the labelling [25]. As explained in [7], $\phi(x_i, x_j)$ is given by the Potts model. If pixel i and pixel j have the same label, the penalty term is equal to zero, and if not, it is equal to one.

$$P(x_i, x_j) = \phi(x_i, x_j) \underbrace{\sum_{m=1}^M \omega^{(m)} k^{(m)}(\mathbf{f}_i, \mathbf{f}_j)}_{k(\mathbf{f}_i, \mathbf{f}_j)} \quad (3)$$

As Eq. 3 shows, each $k^{(m)}$ is the Gaussian kernel, which is depends on the feature vectors $\mathbf{f}_i, \mathbf{f}_j$ of pixels i, j , and is weighted by $\omega^{(m)}$. In [7], it uses contrast-sensitive two-kernel potentials, defined in terms of the color vectors I_i and I_j and positions p_i and p_j . It is shown as Eq. 4.

$$k(\mathbf{f}_i, \mathbf{f}_j) = \underbrace{\omega_1 \exp\left(-\frac{\|p_i - p_j\|^2}{2\sigma_\alpha^2} - \frac{\|I_i - I_j\|^2}{2\sigma_\beta^2}\right)}_{\text{appearance kernel}} + \underbrace{\omega_2 \exp\left(-\frac{\|p_i - p_j\|^2}{2\sigma_\gamma^2}\right)}_{\text{smoothness kernel}} \quad (4)$$

The first appearance kernel depends on both pixel positions (denoted as p) and pixel color intensities (denoted as I). The second smoothness kernel only depends on pixel positions. And the parameters $\sigma_\alpha, \sigma_\beta$ and σ_ω control the scale of Gaussian kernels. The first kernel forces pixels with similar color and position to have similar labels, while the second kernel only considers spatial proximity when enforcing smoothness [23].

4) *VGG-16*: Simonyan et al. propose VGG-16, which not only achieves the state-of-the-art accuracy on ILSVRC 2014 classification and localisation tasks, but is also applicable to other image recognition data sets, where they achieve excellent performance even when used as a part of a relatively simple pipelines [6]. The architecture of VGG-16 is shown in Fig. 4.

III. MULTI-SCALE CNN-CRF MODEL

A. Pixel-level Training

In pixel-level training, our novel multilevel CNN-CRF framework is introduced. In our data set, there are many objects of various sizes. As Fig. 5 shows, we can easily find the EM shapes in different categories are completely different. Considering the current U-Net is difficult to adapt to this situation, thus we propose novel methods to optimize the adaptability of U-Net.

As the U-Net structure shown in Fig. 2, we can find the receptive field of U-Net is limited. In order to optimize the adaptability of U-Net, the direct way is using convolution filters of different sizes, just as Inception does. We propose BLOCK-I, which incorporates $1 \times 1, 3 \times 3, 5 \times 5$ and

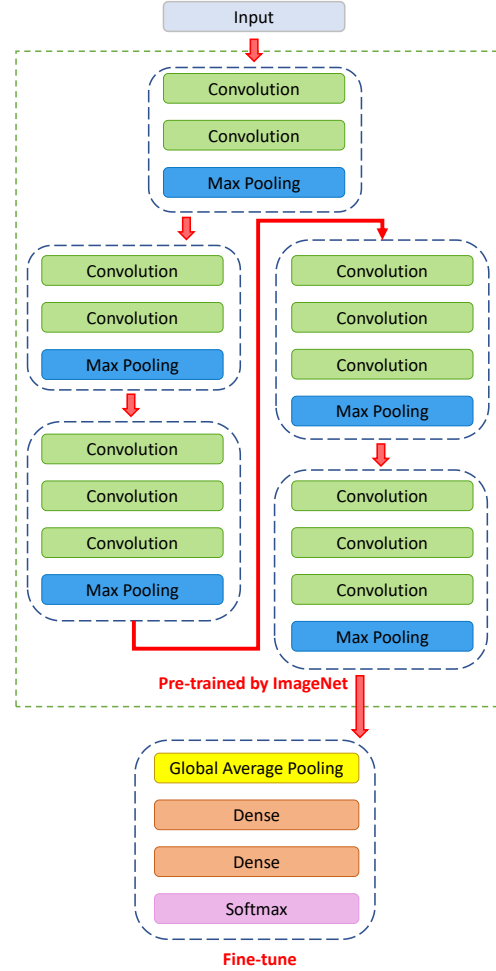


Fig. 4. The architecture of VGG-16 network.

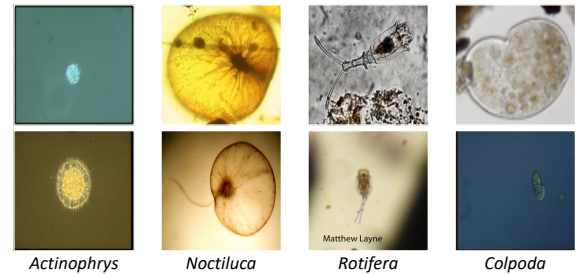


Fig. 5. The variety of the object sizes in EM images.

7×7 convolution operations in parallel, as shown in Fig. 6. Although this approach can help the network to improve the adaptability, it also makes more parameters.

Inspired by Inception-V2 [21], a 5×5 convolution filter actually resembles a sequence of two 3×3 convolution filters. Likewise, a 7×7 convolution filter can be replaced by a sequence of three 3×3 convolution filters. In [26], the concatenate operation is used to concatenate the outputs after the first convolution operation and the second convolution operation with the output of the third convolution operation in a sequence of three 3×3 convolution operations to obtain the result which resembles the interaction result of $3 \times 3, 5 \times 5$ and

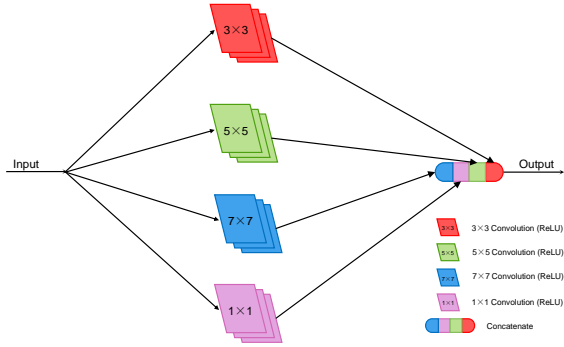


Fig. 6. The architecture of BLOCK-I.

7×7 convolution operations. Therefore, we apply this thought to optimize BLOCK-I, and we get a novel architecture called BLOCK-II. BLOCK-II is shown as Fig. 7. Compared with BLOCK-I, this architecture can reduce parameters.

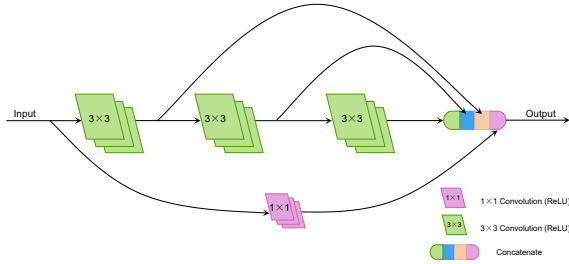


Fig. 7. The architecture of BLOCK-II.

Although the parameters of BLOCK-II is quite less than BLOCK-I, there is still some spaces for improvement in this architecture. As we mentioned about Inception-V3, a 3×3 convolution filter can also be replaced by a sequence of 1×3 and 3×1 convolution filters. We apply this thought in BLOCK-III, which is shown as Fig. 8. The experiments show that this approach can effectively reduce the memory requirement and achieve well performed results.

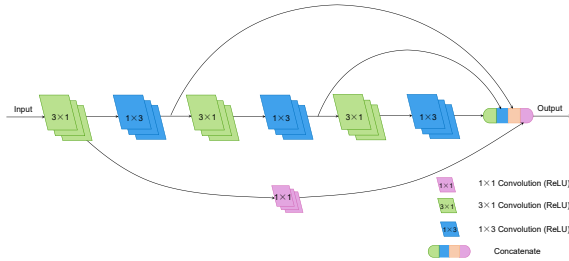


Fig. 8. The architecture of BLOCK-III.

Finally, We provide the whole architecture of our network mU-Net in Fig. 9. Because of the least memory requirement of BLOCK-III, we deploy BLOCK-III in mU-Net architecture in our final method. In addition, we add a batch normalization layer [27] after each convolution layer and convolution transpose layer. For short, mU-Net with BLOCK-X is abbreviated as “mU-Net-BX”. The details of mU-Net-BXs are provided in Table. I.

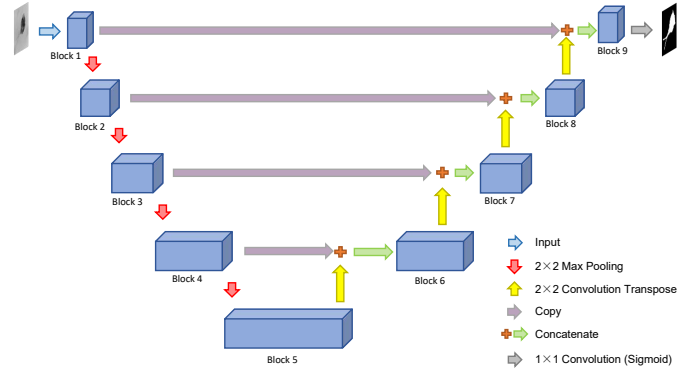


Fig. 9. The architecture of mU-Net.

B. Patch-level Training

In our patch-level training, we use our data set to fine-tune the VGG-16 [6], which is pre-trained on a large-scale image data set ImageNet [28].

1) *Fine-tune Pre-trained VGG-16*: It is proved the use of VGG-16 pre-trained on ImageNet can be useful for classification tasks through the concept of transfer learning and fine-tuning in [29]. In our framework, the patch-level segmentation is actually a classification task.

To fine-tune the pre-trained model, we mesh the training EM images into patches of 8×8 pixels. The examples are shown in Fig. 10. There are two reasons for using patches of 8×8 pixels. First, all the EM images sizes are converted into 256×256 pixels where 256 can only be divisible by 2, 4, 8, 16, 32, 64, 128 or 256. Second, the patches, which are too large or too small, make no sense for the patch-level segmentation, because small patches cannot obtain details of EMs and large patches will result in rough segmentation results. We provide some examples of patches of different sizes in the original EM images in Fig. 11. As we can see, patches of 2×2 and 4×4 pixels are too small to cover the details of EMs, and patches of 16×16 pixels are too large for the images.

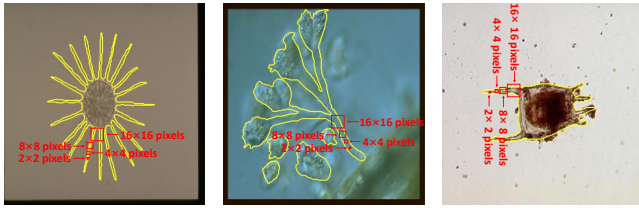


Fig. 10. Examples of patches for pixel-level training (The top and third rows are grayscale image patches; and the second and bottom rows are their corresponding GT images).

After that, we divide these patches into two categories: With Object and Without Object. The criterion for dividing is the area of object in each patch. If the area is more than half of the patch, we will give the label of With Object to this patch. If not, the label will be Without Object. Finally, we apply data augmentation to make the number of patches in two categories balanced, and use the balanced data to train a classification model through pre-trained VGG-16 based on ImageNet and fine-tuning the dense layers of VGG-16.

TABLE I
DETAILS OF MU-NET ARCHITECTURE WITH DIFFERENT BLOCKS.

Block	Model			Filter Number	Block	Model			Filter Number
	mU-Net-B1	mU-Net-B2	mU-Net-B3			mU-Net-B1	mU-Net-B2	mU-Net-B3	
Block 1 & Block 9	Con2D(3,3)	Con2D(3,3)	Con2D(3,1) Con2D(1,3)	16	Block 2 & Block 8	Con2D(3,3)	Con2D(3,3)	Con2D(3,1) Con2D(1,3)	32
	Con2D(5,5)	Con2D(3,3)	Con2D(3,1) Con2D(1,3)			Con2D(5,5)	Con2D(3,3)	Con2D(3,1) Con2D(1,3)	
	Con2D(7,7)	Con2D(3,3)	Con2D(3,1) Con2D(1,3)			Con2D(7,7)	Con2D(3,3)	Con2D(3,1) Con2D(1,3)	
	Con2D(1,1)	Con2D(1,1)	Con2D(1,1)			Con2D(1,1)	Con2D(1,1)	Con2D(1,1)	
Block 3 & Block 7	Con2D(3,3)	Con2D(3,3)	Con2D(3,1) Con2D(1,3)	64	Block 4 & Block 6	Con2D(3,3)	Con2D(3,3)	Con2D(3,1) Con2D(1,3)	128
	Con2D(5,5)	Con2D(3,3)	Con2D(3,1) Con2D(1,3)			Con2D(5,5)	Con2D(3,3)	Con2D(3,1) Con2D(1,3)	
	Con2D(7,7)	Con2D(3,3)	Con2D(3,1) Con2D(1,3)			Con2D(7,7)	Con2D(3,3)	Con2D(3,1) Con2D(1,3)	
	Con2D(1,1)	Con2D(1,1)	Con2D(1,1)			Con2D(1,1)	Con2D(1,1)	Con2D(1,1)	
Block 5	Con2D(3,3)	Con2D(3,3)	Con2D(3,1) Con2D(1,3)	256					
	Con2D(5,5)	Con2D(3,3)	Con2D(3,1) Con2D(1,3)						
	Con2D(7,7)	Con2D(3,3)	Con2D(3,1) Con2D(1,3)						
	Con2D(1,1)	Con2D(1,1)	Con2D(1,1)						



(a) *Actinophrys* (b) *Epistylis* (c) *K. Quadrata*

Fig. 11. The examples of the image patches of different sizes. The yellow outlines show the regions of EMs in GT images. The red arrows point out the image patches of different sizes.

C. Pixel-level Post-processing

In our pixel-level segmentation, after getting the segmentation results from mU-Net-B3, we convert the results into binary images, where the foreground is marked as 1 (white) and the background is marked as 0 (black), and use the binary images as the initial matrices of denseCRF. It can effectively obtain the global informations in images to optimize the segmentation results.

D. Patch-level Post-processing

In our patch-level segmentation, we use the predicted labels generated by VGG-16 to reconstruct the segmentation results. In order to remove the useless portions of the patch-level segmentation results, we built up the buffers by using the pixel-level post-processing (denseCRF) results. The process is shown in Fig. 12. The way to make buffers is applying dilate operation to the denseCRF results for thirty times. After that, we use these images as weight matrices to apply on the patch-level results. Only the patch-level segmentation results

in the buffers are retained, and the segmentation results outside the buffers are erased. This approach can effectively help to denoise.

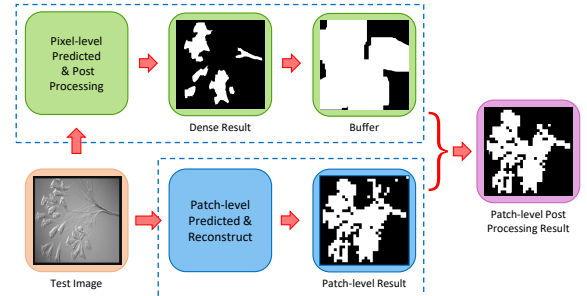


Fig. 12. The workflow of the patch-level post-processing.

E. Segmentation Results Fusion and Presentation

After obtaining the segmentation results of pixel-level and patch-level, respectively, the final segmentation results are generated by combining these two kinds of segmentation results. For convenience of observation, the segmentation results of pixel-level and patch-level are plotted on the original images in the form of masks of different colors. The masks of pixel-level are red, the masks of patch-level are fluorescent green, and the overlapped parts of pixel-level and patch-level segmentation results are yellow. There are some examples shown in Fig. 25.

IV. EXPERIMENTS AND ANALYSIS

A. Experimental setting

1) *Image Data Set*: In our work, we use *Environmental Microorganism Data Set 5th Version* (EMDS-5), which is a

newly released version of EMDS series [30], containing 21 classes of EM as shown in Fig. 13. Each EM class contains 20 original microscopic images and their corresponding GT images, thus the data set includes 420 scenes. Owing to the microscopic images have multifarious sizes, we convert all the image sizes into 256×256 pixels uniformly.

2) *Training, Validation and Test Data Setting*: We randomly divide each class of EMDS-5 into training data set, validation data set and test data set in a ratio of 1:1:2. In our pixel-level training, data augmentation can make up the lack of training images. Refer to the strategy proposed in [19], we augment the 105 training images with rotations by 0, 90, 180, 270 degrees and mirroring, which results in 840 images for training. In our patch-level training, we mesh 105 training images and their corresponding GT images into patches (8×8 pixels), and 107520 patches are obtained. These patches are divided into two categories: With Object and Without Object. We find that the numbers of patches in these two categories are inconsistent. The first category (With Object) has 18575 patches, another category (Without Object) has 88945 patches. To optimize this situation, we employ data augmentation to the first category (With Object). We augment the 18575 patches in the first category (Without Object) with rotations by 0, 90, 180, 270 degrees and mirroring which result in 148600 patches. Then we randomly choose 88945 patches to replace the data in the first category (With Object).

3) *Experimental Environment*: The experiment is conducted by Python 3. The models are implemented using Keras [31] framework with Tensorflow [32] as backend. In our experiment, we use a workstation with Intel(R) Core(TM) i7-8700 CPU with 3.20GHz, 32GB RAM and NVIDIA GEFORCE RTX 2080 8GB.

4) *Pixel-level Implementation Details*: In our pixel-level segmentation, the task of the segmentation is to predict the individual pixels whether they represent a point of foreground or background. Actually, this task can be seen as a pixel-level binary classification problem. Hence, as the loss function of the network we simply take the binary cross-entropy function and minimize it [26]. Besides, we use Adam optimizer with 1.5×10^{-4} learning rate in our training process. The models are trained for 50 epochs using Adam optimizer.

5) *Patch-level Implementation Details*: In our patch-level training process, we employ the pre-trained VGG-16 as the core and fine-tune the dense layers of VGG-16. As the Fig. 4 shows, the last layer is softmax. The categorical cross-entropy function is the loss function of choice for softmax output units. In addition, Adam optimizer with 1.0×10^{-4} learning rate is used in VGG-16. The pre-trained model is trained for 15 epochs.

B. Evaluation Metric

In our previous work [3], Recall and Accuracy are used to measure the segmentation results. Besides that, we employ Dice, Jaccard and VOE (volumetric overlap error) to evaluate the segmentation results in this paper [33]. The definitions of these evaluation metrics are provided in Tab. II. V_{pred} represents the foreground that predicted by the model. V_{gt} means the foreground in a ground truth image.

TABLE II
THE DEFINITIONS OF EVALUATION METRICS FOR IMAGE SEGMENTATION. TP (TRUE POSITIVE), FN (FALSE NEGATIVE), FP (FALSE POSITIVE) AND TN (TRUE NEGATIVE).

Metric	Definition	Metric	Definition
Dice	$\text{Dice} = \frac{2 \times V_{\text{pred}} \cap V_{\text{gt}} }{ V_{\text{pred}} + V_{\text{gt}} }$	Jaccard	$\text{Jaccard} = \frac{ V_{\text{pred}} \cap V_{\text{gt}} }{ V_{\text{pred}} \cup V_{\text{gt}} }$
Recall	$\text{Recall} = \frac{\text{TP}}{\text{TP} + \text{FN}}$	Accuracy	$\text{Accuracy} = \frac{\text{TP} + \text{TN}}{\text{TP} + \text{FN} + \text{FP} + \text{TN}}$
VOE	$\text{VOE} = 1 - \frac{ V_{\text{pred}} \cap V_{\text{gt}} }{ V_{\text{pred}} \cup V_{\text{gt}} }$		

From Tab. II, we can find the higher the values of the first four metrics (Dice, Jaccard, Recall and Accuracy) are, the better the segmentation results are. On the contrary, the lower the value of the final metric (VOE) is, the better the segmentation result is.

C. Evaluation of Pixel-level Segmentation

Because the pixel-level segmentation methods are discussed in detail above, we mainly introduce comparisons between U-Net [20], the models we proposed, the existing segmentation methods mentioned in Sec. II-A and the segmentation result of our previous work [3] in this section.

1) *Evaluation of Different BLOCKs*: In this part, we make comparisons between different mU-Net-BXs and U-Net from memory requirement, time requirement and segmentation performance.

Memory Requirement: The memory requirements of U-Net and mU-Net-BXs are provided in Fig. 14. As we can see, the memory requirements of U-Net, mU-Net-B1, mU-Net-B2 and mU-Net-B3 are 355 MB, 407 MB, 136 MB and 103 MB, respectively. Obviously, mU-Net-B3 has the lowest memory requirement.

Time Requirement: For 840 training images and 210 testing images, the time requirements of U-Net and these improved models, which include training and average testing time, are provided in Table.III. The training time of U-Net, mU-Net-B1, mU-Net-B2 and mU-Net-B3 are 35.756 minutes, 78.235 minutes, 28.53 minutes and 36.521 minutes, respectively. The average testing time of U-Net, mU-Net-B1, mU-Net-B2 and mU-Net-B3 are 0.045 seconds, 0.134 seconds, 0.091 seconds and 0.148 seconds, respectively. We can find that all these networks have a short test time that is less than 0.15s, showing their feasibility in the practical EM image segmentation task.

TABLE III
THE TIME REQUIREMENT OF U-NET AND MU-NET-BXs.

Time Requirement	Model			
	U-Net	U-Net-B1	U-Net-B2	U-Net-B3
Training	35.76min	78.24min	28.53min	36.52min
Average Testing	0.045s	0.134s	0.091s	0.148s

Segmentation Performance: As the workflow shown in Fig. 1, the evaluation indexes of all improved models are

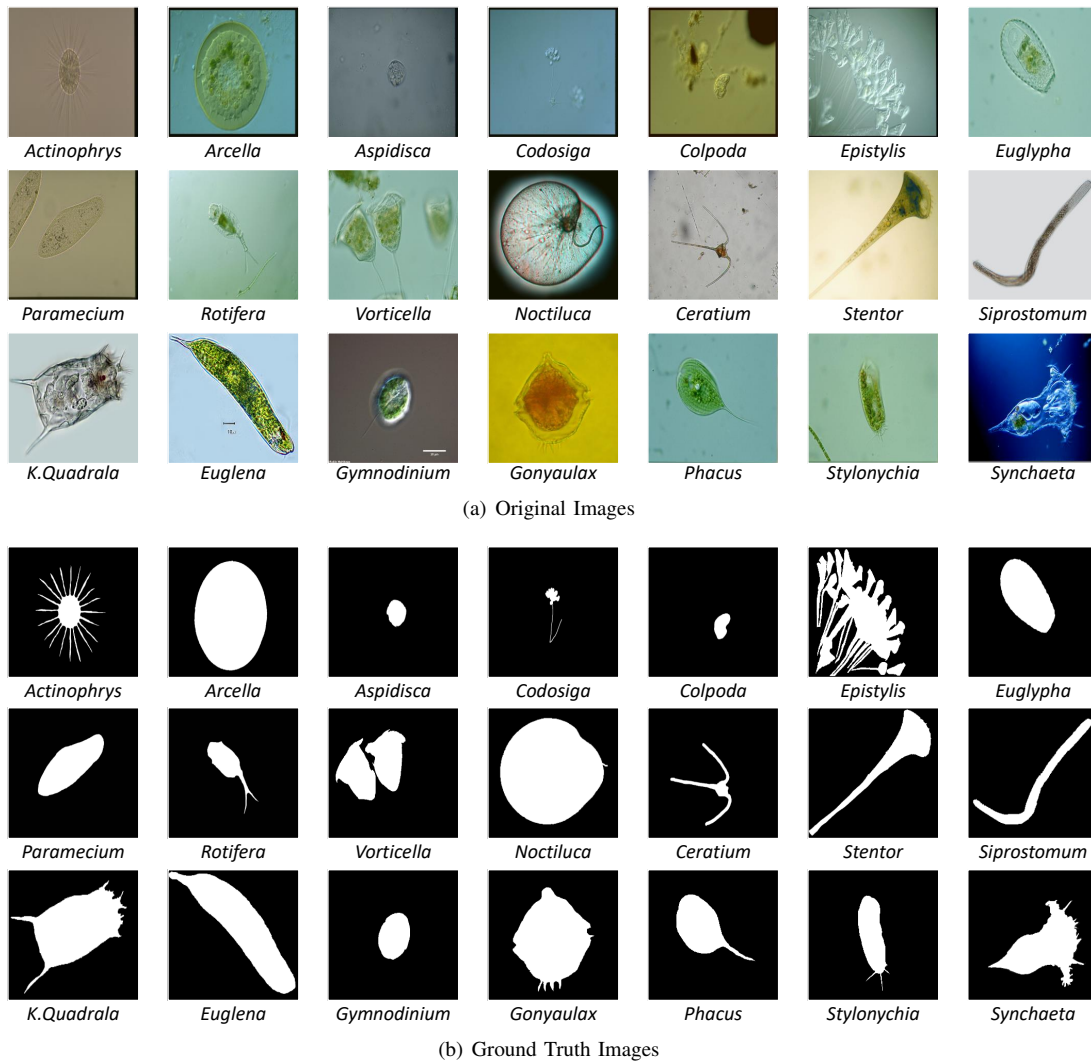


Fig. 13. Examples of the images in EMDS-5. (a) provides the original EM images and (b) provides the corresponding GT images.

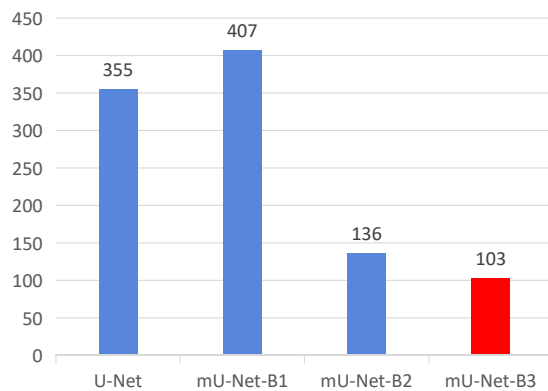


Fig. 14. The memory requirements of U-Net and mU-Net-BXs. (In MB)

provided with denseCRF as the post-processing. The overall segmentation performance of U-Net and these improved models are shown in Fig. 15. As we can see, all the improved models make better performance than U-Net. Compared with U-Net, the average Dice values of all the improved models

are increased more than by 1.8%, and in particular, the improvements of mU-Net-B1 and mU-Net-B2 are more than 2%. The average Jaccard values of mU-Net-B1, mU-Net-B2 and mU-Net-B3 make 2.89%, 2.75% and 2.32% improvements, respectively. Likewise, the improvements of the average Recall values made by these improved models are 4.98%, 4.91% and 4.85%, respectively, and for the average Accuracy values, the improvements of these improved models are 0.65%, 0.34% and 0.15%, respectively. The average VOE values of the improved models are reduced by 2.89%, 2.75% and 2.32%, respectively.

Summary: From above, we can find all the improved models make better segmentation performance than U-Net. Compared with mU-Net-B1 and mU-Net-B2, mU-Net-B3 has the lowest memory requirement, relatively low time requirement and the similar performance, so it has a big potential in the practice of EM image segmentation work.

After evaluating the overall performances of these methods, we also provide the detailed indexes and segmentation results examples of each category of EM under these methods in Table. IV and Fig. 16, respectively.

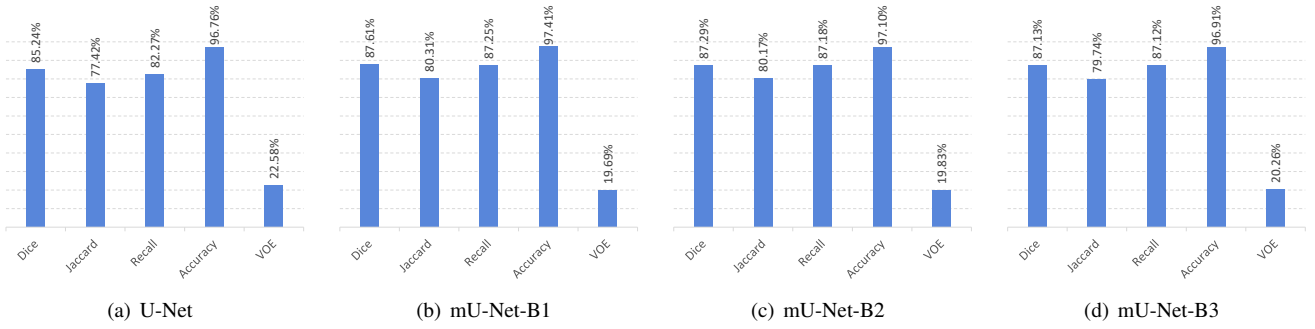


Fig. 15. The average evaluation indexes of U-Net, mU-Net-BXs and mU-Net-B3 with denseCRF.

TABLE IV

THE AVERAGE INDEXES FOR EACH CATEGORY OF EM GENERATED BY U-NET, MU-NET-BXS. FOR SHORT, IN THE FOLLOWING TABLE, MU-NET-B1, MU-NET-B2 AND MU-NET-B3 ARE ABBREVIATED AS B1, B2 AND B3, RESPECTIVELY.

EM	Methods	Evaluation Metrics					EM	Methods	Evaluation Metrics					EM	Methods	Evaluation Metrics				
		Dice	Jaccard	Recall	Accuracy	VOE			Dice	Jaccard	Recall	Accuracy	VOE			Dice	Jaccard	Recall	Accuracy	VOE
1	U-Net	71.80	57.47	59.13	97.53	42.53	8	U-Net	92.77	87.46	93.74	97.84	12.54	15	U-Net	93.06	87.23	91.36	97.38	12.77
	B1	71.30	56.76	59.19	97.41	43.24		B1	94.05	89.39	94.90	98.19	10.61		B1	92.96	87.26	92.26	97.46	12.74
	B2	72.04	57.77	59.46	97.56	42.23		B2	94.51	89.98	95.80	98.29	10.02		B2	93.71	88.30	92.12	97.72	11.70
	B3	72.16	57.86	59.52	97.57	42.14		B3	94.59	90.00	96.97	98.23	10.00		B3	93.12	87.25	91.62	97.49	12.75
2	U-Net	94.87	91.18	92.54	97.50	8.82	9	U-Net	86.57	80.98	83.51	97.55	19.02	16	U-Net	89.80	82.23	84.41	97.59	17.77
	B1	97.47	95.24	98.28	98.63	4.76		B1	88.99	82.23	88.72	97.11	17.77		B1	91.90	85.43	87.18	98.06	14.57
	B2	95.04	91.15	96.52	97.19	8.85		B2	92.04	86.17	89.02	98.15	13.83		B2	92.68	86.62	86.83	98.17	13.38
	B3	97.69	95.69	98.67	98.71	4.31		B3	89.38	82.49	90.88	97.01	17.51		B3	92.40	86.18	87.93	98.22	13.82
3	U-Net	94.06	88.86	92.19	99.70	11.14	10	U-Net	91.36	84.30	95.13	98.97	15.70	17	U-Net	89.28	83.16	94.22	97.95	16.84
	B1	93.02	87.09	93.11	99.62	12.91		B1	93.97	88.79	95.52	99.02	11.21		B1	86.76	79.87	95.46	97.84	20.13
	B2	94.25	89.25	93.44	99.71	10.75		B2	94.17	89.23	95.87	98.94	10.77		B2	85.77	79.15	95.18	97.48	20.85
	B3	94.30	89.38	92.82	99.71	10.62		B3	94.71	90.01	95.52	99.34	9.99		B3	84.94	78.99	95.22	96.79	21.01
4	U-Net	48.83	38.24	44.24	96.64	61.76	11	U-Net	88.48	82.47	83.70	92.27	17.53	18	U-Net	93.08	87.27	88.16	95.07	12.73
	B1	58.16	44.90	57.02	97.12	55.10		B1	96.51	93.41	95.31	97.19	6.59		B1	94.89	90.35	91.69	96.48	9.65
	B2	60.76	47.66	57.68	97.31	52.34		B2	96.10	92.63	94.67	96.91	7.37		B2	94.23	89.21	90.35	96.07	10.79
	B3	59.20	46.29	60.44	96.68	53.71		B3	92.08	86.35	87.49	93.95	13.65		B3	94.12	88.99	90.18	95.82	11.01
5	U-Net	87.46	78.83	91.19	97.25	21.17	12	U-Net	83.32	73.21	76.63	96.91	26.79	19	U-Net	91.56	85.20	85.43	98.37	14.80
	B1	86.38	77.74	95.20	98.09	22.26		B1	81.60	72.11	79.57	96.65	27.89		B1	93.63	88.37	88.66	98.72	11.63
	B2	85.44	77.88	94.72	97.90	22.12		B2	82.89	73.45	82.73	96.86	26.55		B2	93.37	87.68	87.95	98.41	12.32
	B3	82.28	72.93	91.74	97.22	27.07		B3	86.78	77.63	80.49	97.53	22.37		B3	90.97	84.36	85.12	97.99	15.64
6	U-Net	55.43	40.56	50.04	89.00	59.44	13	U-Net	88.76	80.63	84.50	97.25	19.37	20	U-Net	80.01	68.72	70.06	93.57	31.28
	B1	69.29	53.89	72.69	90.74	46.11		B1	92.23	85.80	91.60	98.02	14.20		B1	89.79	82.30	83.22	96.17	17.70
	B2	63.70	48.62	75.06	86.93	51.38		B2	87.19	79.86	91.13	95.22	20.14		B2	89.43	81.59	83.25	96.19	18.41
	B3	64.01	48.94	76.74	87.11	51.06		B3	89.87	83.24	92.61	96.44	16.76		B3	87.32	79.11	80.82	95.27	20.89
7	U-Net	90.11	82.93	93.82	98.41	17.07	14	U-Net	84.62	74.52	83.31	97.76	25.48	21	U-Net	94.86	90.32	90.49	97.52	9.68
	B1	88.53	80.59	97.21	97.99	19.41		B1	83.60	74.85	84.45	97.60	25.15		B1	94.71	90.08	90.93	97.43	9.92
	B2	90.33	82.99	96.66	98.44	17.01		B2	79.97	73.21	80.36	97.85	26.79		B2	95.38	91.26	92.02	97.80	8.74
	B3	88.96	81.04	98.21	98.16	18.96		B3	85.68	76.69	84.58	98.06	23.31		B3	95.24	91.01	91.91	97.73	8.99

2) *Comparison with Other Methods:* In this part, we conduct some comparative experiments on the task of EM segmentation. During the experiments, we mainly adopt some representative segmentation methods mentioned in Sec. II-A1 and Sec. II-A2, including Otsu, Canny, Watershed, MRF and k -means. During the experiments, because the results are often insufficient, we need some post-processing for the results. In order to show better segmentation results of these methods, we uniformly use the same post-processing operations. In order to evaluate the overall performances of these methods, we provide the average evaluation indexes of these methods in Fig. 17.

From Fig. 17, we can find none of the methods perform

as well as the proposed methods. But we can find the recall values in Fig. 17 are higher than the recall values in Fig. 15. This is because some of the segmentation results generated by these methods have a lot of background parts divided into the foreground. From Table. II, we can realize that as long as the foreground in the segmentation result contains the entire real foreground in GT images, the value of recall is 1 regardless of whether the over-segmentation problem is existing or not. Therefore, we should not judge the segmentation results by Recall alone.

In order to better observe the performance of these methods, we provide the detailed indexes of the segmentation results of each category of EM under these methods in Table. VI.



Fig. 16. An example of GT images and segmentation results for each category of EMs by U-Net, U-Net-B1, U-Net-B2 and U-Net-B3 (From the left to the right).

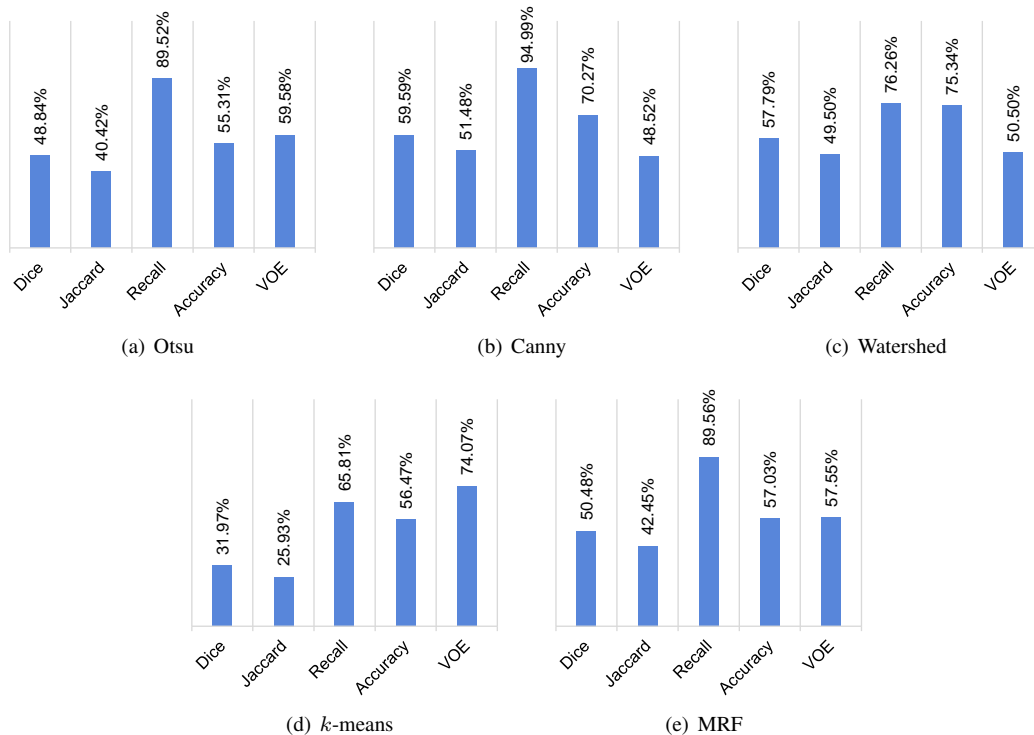


Fig. 17. The average evaluation indexes of Otsu, Canny, Watershed, *k*-means and MRF.

Besides, we also provide the examples of the segmentation results under these methods in Fig. 18.

3) *Comparison with Our Previous Work*: In our previous work [3], the EMDS-4 data set we used contains only 20 categories. The 17th category (*Gymnodinium*), which used in this paper, is excluded in our previous work. Besides, we only use Average Recall and Overall Accuracy to evaluate the segmentation performance in our previous work. Therefore, we provide the evaluation indexes of the segmentation results obtained by mU-Net-B3 with denseCRF without the 17th category. Furthermore, in our previous work, there are six models for segmentation: Per-pixel RF (noEdges), CRF with Potts pairwise potentials (Potts), CRF with contrast-sensitive Potts model (PottsCS), fully connected CRF with Gaussian pairwise potentials (denseCRF), fully connected CRF on segmentation results by the original DeepLab method [23] (denseCRForg), fully convolutional network (FCN). We provide the Average Recall and Overall Accuracy values of mU-Net-B3 with denseCRF (XB3denseCRF) and our previous models in Fig. 19. It can be found from Fig. 19 that compared with the previous models, the Average Recall is improved by more than 7%, and the increase of Overall Accuracy increases by at least 1%. From that, we can realize mU-Net-B3 with denseCRF we proposed in this paper performs better than the models in our previous work.

D. Evaluation of Patch-level Segmentation

Although mU-Net-B3 with Dense CRF perform well on the segmentation task for most categories of EM, there are still some shortages. For example, as shown in Fig 16(f), mU-Net-B3 is not able to segment the whole object, leading to an

under-segmentation result. Therefore, we use the patch-level segmentation to make up this shortage.

1) *The Criterion for Assigning the Labels*: In this part, we mainly discuss the criterion for assigning the labels to the patch in training and validation data sets and the determination of buffer size. As we mentioned in Sec. III-B1, we divide the patches into two categories: With Object and Without Object. The criterion for assigning these two labels to the patches is whether the area of the object is more than half of the total area of the patch. There are two reasons for using half area as the criterion. The first reason is that when we choose 0.25 area and 0.75 area as the criteria, the results actually do not make much difference. This is because when we respectively use these three criteria, the number of patches in the two categories actually varies so little. We provide the detailed numbers of the patches in the two categories under different criteria in Table. VI. It means most patches that contain objects are divided into With Object. The second reason is that it can show the lowest loss and the highest accuracy on the validation data set when compared with 0.25 and 0.75 area, respectively. The loss values of using 0.25 area, 0.5 area, 0.75 area as the criterion are 26.74%, 26.37% and 27.38%, respectively. The accuracy values of using 0.25 area, 0.5 area, 0.75 area as the criterion are 90.24%, 90.33% and 90.12%, respectively. In addition, we provide some segmentation results under different criteria as examples in Fig. 20.

2) *The Determination of Buffer Size*: From Fig. 20, we can find that the patch-level segmentation results contain a lot of noises around the objects we need to segment. We only want to retain the useful parts of the patch-level segmentation results and remove the useless parts. The direct way is establishing

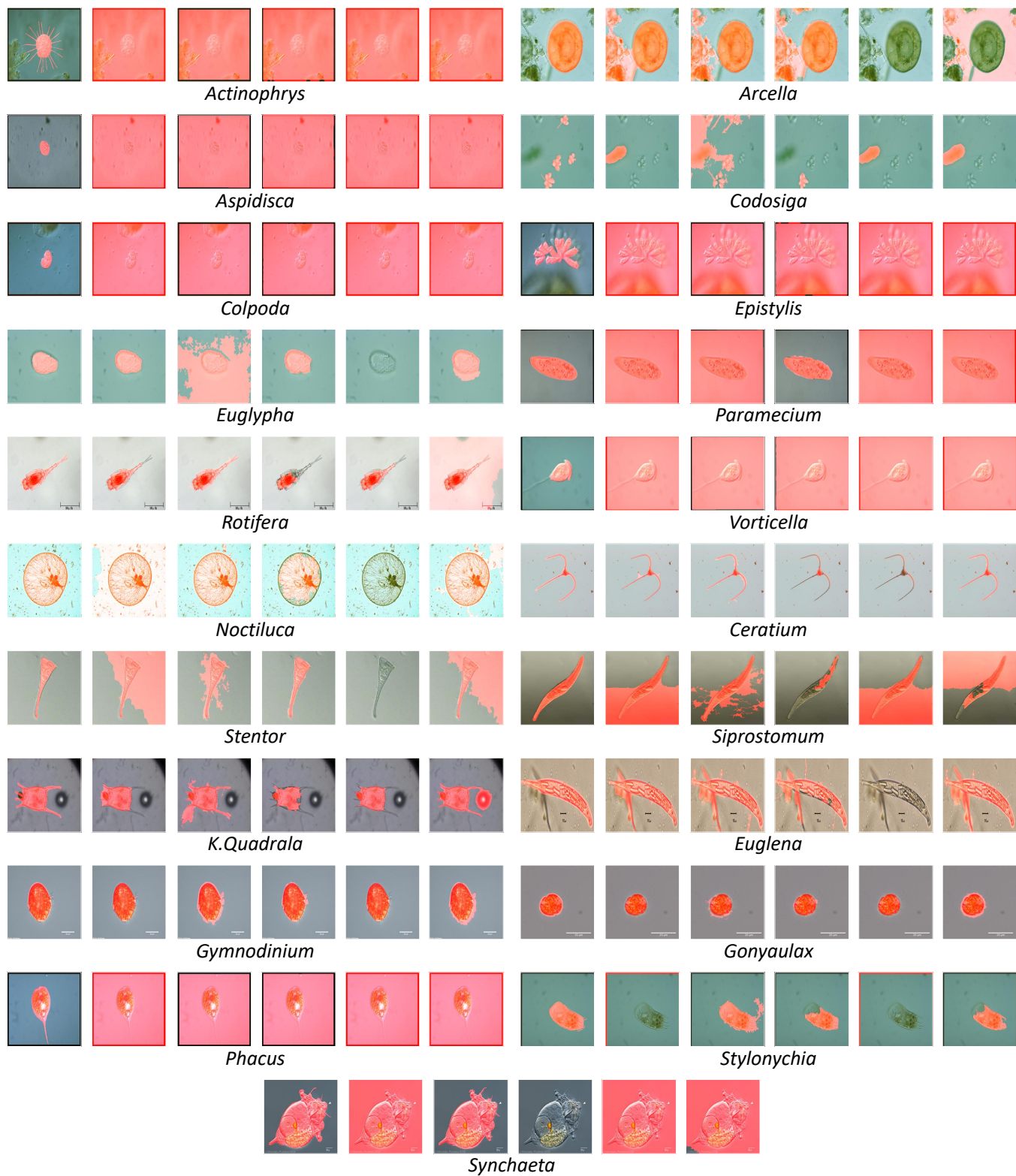


Fig. 18. An example of GT images and segmentation results for each category of EM generated by Otsu, Canny, Watershed, k -means and MRF methods (From the left to the right).

TABLE V
THE AVERAGE INDEXES FOR EACH CATEGORY OF EM GENERATED BY OTSU, CANNY, WATERSHED, k -MEANS AND MRF.

EM	Methods	Evaluation Metrics					EM	Methods	Evaluation Metrics					EM	Methods	Evaluation Metrics				
		Dice	Jaccard	Recall	Accuracy	VOE			Dice	Jaccard	Recall	Accuracy	VOE			Dice	Jaccard	Recall	Accuracy	VOE
1	Otsu	31.12	24.88	81.96	41.41	75.12	8	Otsu	48.37	38.58	98.88	45.03	61.42	15	Otsu	81.89	72.00	91.81	86.40	28.00
	Canny	27.42	19.37	99.16	36.52	80.63		Canny	56.84	45.71	99.04	59.01	54.29		Canny	90.24	82.68	97.55	96.33	17.32
	Watershed	32.05	26.13	83.53	44.12	73.87		Watershed	64.85	55.60	85.37	71.92	44.40		Watershed	86.87	77.41	87.17	95.14	22.59
	k -means	14.73	10.85	67.74	40.37	89.15		k -means	14.27	8.53	50.00	50.66	91.47		k -means	53.16	45.87	61.56	77.84	54.13
	MRF	30.79	24.17	95.69	33.50	75.83		MRF	49.80	40.69	90.44	48.86	59.31		MRF	78.00	68.09	97.83	83.00	31.91
2	Otsu	73.32	63.24	98.64	71.46	36.76	9	Otsu	70.77	62.37	91.17	82.17	37.63	16	Otsu	58.89	48.05	77.64	75.02	51.95
	Canny	76.29	66.33	99.13	77.18	33.67		Canny	59.88	53.94	68.78	89.70	46.06		Canny	65.46	54.89	97.17	77.66	45.11
	Watershed	67.02	58.11	85.35	74.54	41.89		Watershed	69.53	57.41	73.35	91.25	42.59		Watershed	83.95	76.86	89.09	88.97	23.14
	k -means	52.41	47.40	68.88	70.18	52.60		k -means	70.40	63.18	79.46	88.32	36.82		k -means	35.76	29.06	52.81	73.97	70.94
	MRF	65.40	57.31	89.97	63.60	42.69		MRF	62.29	54.19	96.48	72.24	45.81		MRF	72.88	62.65	86.65	82.23	37.35
3	Otsu	4.49	2.31	89.49	14.31	97.69	10	Otsu	40.02	30.44	92.00	49.12	69.56	17	Otsu	30.04	23.52	97.30	29.84	76.48
	Canny	13.90	10.14	99.96	25.33	89.86		Canny	39.67	29.82	99.78	51.99	70.18		Canny	68.81	60.51	88.19	87.95	39.49
	Watershed	12.22	9.87	69.11	44.02	90.13		Watershed	52.79	46.33	81.29	69.19	53.67		Watershed	75.71	70.45	84.80	91.40	29.55
	k -means	4.38	2.25	90.00	11.97	97.75		k -means	26.83	21.05	60.11	58.32	78.95		k -means	22.88	16.54	89.23	26.35	83.46
	MRF	4.37	2.24	90.00	12.80	97.76		MRF	39.99	30.49	99.77	49.66	69.51		MRF	71.57	62.06	93.71	80.57	37.94
4	Otsu	4.49	2.32	90.00	11.32	97.68	11	Otsu	62.33	47.70	98.31	53.08	52.30	18	Otsu	73.25	63.89	93.31	68.78	36.11
	Canny	7.08	3.76	96.78	17.31	96.24		Canny	96.33	93.08	98.69	97.26	6.92		Canny	93.34	87.71	91.57	95.46	12.29
	Watershed	7.11	4.17	62.70	41.28	95.83		Watershed	81.31	70.81	76.38	88.34	29.19		Watershed	90.56	83.16	90.27	93.60	16.84
	k -means	4.49	2.32	90.00	11.33	97.68		k -means	37.23	26.15	64.81	46.37	73.85		k -means	44.09	35.65	64.40	57.64	64.35
	MRF	4.67	2.41	90.00	13.17	97.59		MRF	75.89	65.49	91.39	74.99	34.51		MRF	71.04	59.07	74.37	77.65	40.93
5	Otsu	31.09	24.68	96.45	29.63	75.32	12	Otsu	71.38	59.30	78.35	87.15	40.70	19	Otsu	40.28	33.47	81.99	48.48	66.53
	Canny	38.84	33.16	99.91	50.24	66.84		Canny	81.01	70.90	94.04	95.34	29.10		Canny	57.15	50.79	97.16	61.44	49.21
	Watershed	35.94	28.92	82.44	58.59	71.08		Watershed	58.03	44.56	49.56	92.10	55.44		Watershed	63.62	56.80	75.32	81.57	43.20
	k -means	14.17	10.11	61.92	41.06	89.89		k -means	49.35	42.78	46.28	92.75	57.22		k -means	40.64	33.98	80.83	49.76	66.02
	MRF	27.95	22.31	96.18	30.01	77.69		MRF	71.41	62.50	95.17	77.90	37.50		MRF	53.15	48.06	95.29	52.46	51.94
6	Otsu	24.72	14.75	90.01	22.98	85.25	13	Otsu	51.66	41.92	93.14	60.62	58.08	20	Otsu	45.84	37.62	66.33	65.49	62.38
	Canny	36.87	23.56	99.25	39.81	76.44		Canny	72.96	59.94	98.60	89.60	40.06		Canny	65.65	55.66	95.10	74.53	44.34
	Watershed	30.75	19.25	81.74	39.34	80.75		Watershed	58.66	45.73	66.26	86.71	54.27		Watershed	53.94	41.84	64.57	73.45	58.16
	k -means	24.72	14.75	90.01	22.99	85.25		k -means	32.19	24.88	66.89	63.76	75.12		k -means	21.65	16.86	43.63	62.27	83.14
	MRF	23.95	14.40	80.01	32.32	85.60		MRF	46.34	37.67	63.34	70.34	62.33		MRF	63.25	54.90	75.36	72.29	45.10
7	Otsu	47.39	41.79	86.30	66.37	58.21	14	Otsu	50.54	40.88	96.80	66.80	59.12	21	Otsu	83.78	75.20	89.96	86.09	24.80
	Canny	50.29	40.19	99.49	64.59	59.81		Canny	58.66	48.92	78.62	91.03	51.08		Canny	94.61	89.95	96.90	97.29	10.05
	Watershed	63.96	55.62	79.39	79.31	44.38		Watershed	50.63	41.24	62.44	87.21	58.76		Watershed	74.09	69.24	71.37	90.15	30.76
	k -means	5.90	3.46	26.19	73.90	96.54		k -means	43.26	35.96	67.48	81.26	64.04		k -means	58.84	52.88	59.87	84.82	47.12
	MRF	34.49	26.47	86.95	50.06	73.53		MRF	37.39	28.75	93.29	48.98	71.25		MRF	75.49	67.62	98.93	71.03	32.38

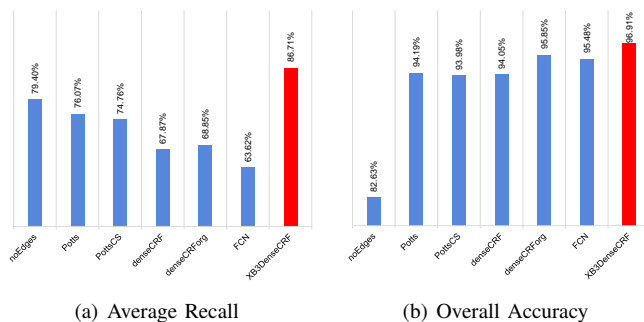


Fig. 19. The average recall and overall accuracy of mU-Net-B3 with denseCRF (XB3DenseCRF) and our previous models.

buffers near the pixel-level segmentation results. There is a

TABLE VI
THE NUMBER OF PATCHES IN DIFFERENT CATEGORIES UNDER DIFFERENT CRITERIA.

Category	Criterion		
	0.25	0.5	0.75
With Object	20670	18575	16823
Without Object	86850	88945	90697

new problem of how to set the size of the buffer. The solution we proposed is combining the patch-level segmentation results under different buffer size settings with pixel-level segmentation results and comparing the combined results with GT images to determine the size of the final buffer based on the performance of evaluation indexes. Furthermore, we make a

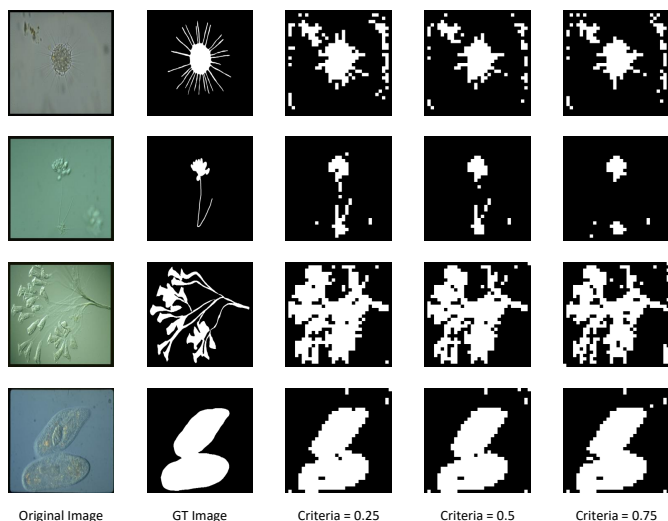


Fig. 20. Patch-level segmentation results under different criteria.

comparison between the buffers with different sizes. It starts with a buffer size of 2 pixels and gradually increases the buffer size by 2 pixels until the buffer size is 40 pixels. After that, the patch-level segmentation results after different buffers processing are combined with the pixel-level segmentation results. Finally, the combined results are compared with GT images to obtain relevant evaluation indexes, which are shown in the Fig. 21.

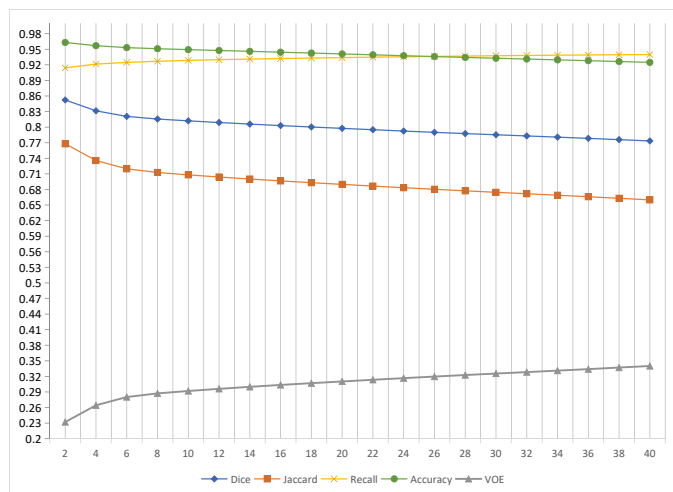


Fig. 21. The evaluation indexes of the combined results under different buffers.

We determine the buffer area size corresponding to the intersection point of Accuracy and Recall in Fig. 21 as the final buffer size setting. The buffer size corresponding to the intersection point is 26 pixels. In addition, we provide the patch-level segmentation results in the form of fluorescent green masks in Fig. 22.

E. Evaluation of combined segmentation results

In order to observe the advantages of combining patch-level segmentation with pixel-level segmentation better, we provide

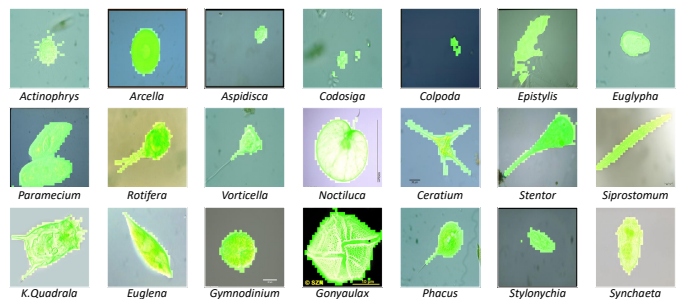


Fig. 22. Examples of patch-level segmentation results with buffer.

some examples and their corresponding evaluation indexes in Fig. 23 and Fig. 24, respectively. We can find that the patch-level segmentation effectively helps to improve the shortages of these pixel-level segmentation.

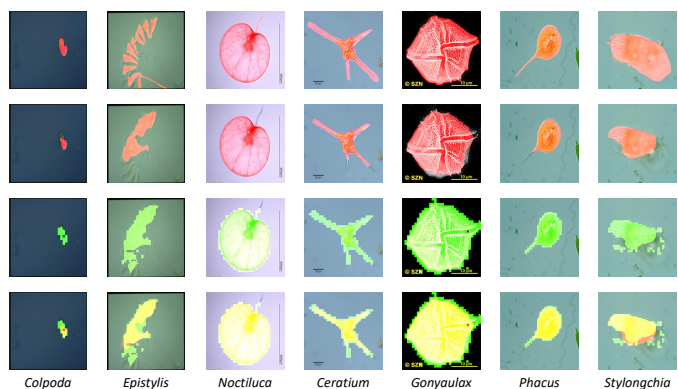


Fig. 23. Examples for proving the validity of combining pixel-level segmentation with patch-level segmentation. From top to bottom, images in each EM represent GT image, pixel-level segmentation result, patch-level segmentation result and combined result, respectively.

F. Segmentation Result Fusion and Presentation

Finally, we provide the combined results of patch-level segmentation results and pixel-level segmentation results in Fig. 25. The yellow parts in the images are the overlapping areas of the patch-level segmentation results (fluorescent green parts) and pixel-level segmentation results (red parts). The purple outline plotted on the images are the GT images.

V. CONCLUSION AND FUTURE WORK

In this paper, we propose a multilevel segmentation method for the EM segmentation task, which includes pixel-level segmentation and patch-level segmentation.

In our pixel-level segmentation, we propose mU-Net-B3 with denseCRF for EM segmentation. It mainly uses the idea of Inception and the use of concatenate operations to reduce the memory requirement. Besides, it also uses denseCRF to obtain global information to further optimize the segmentation results. The proposed method not only performs better than U-Net, but also reduces the memory requirement from 355 MB to 103 MB. In the evaluation of segmentation results generated by this proposed method, the values of evaluation indexes Dice,

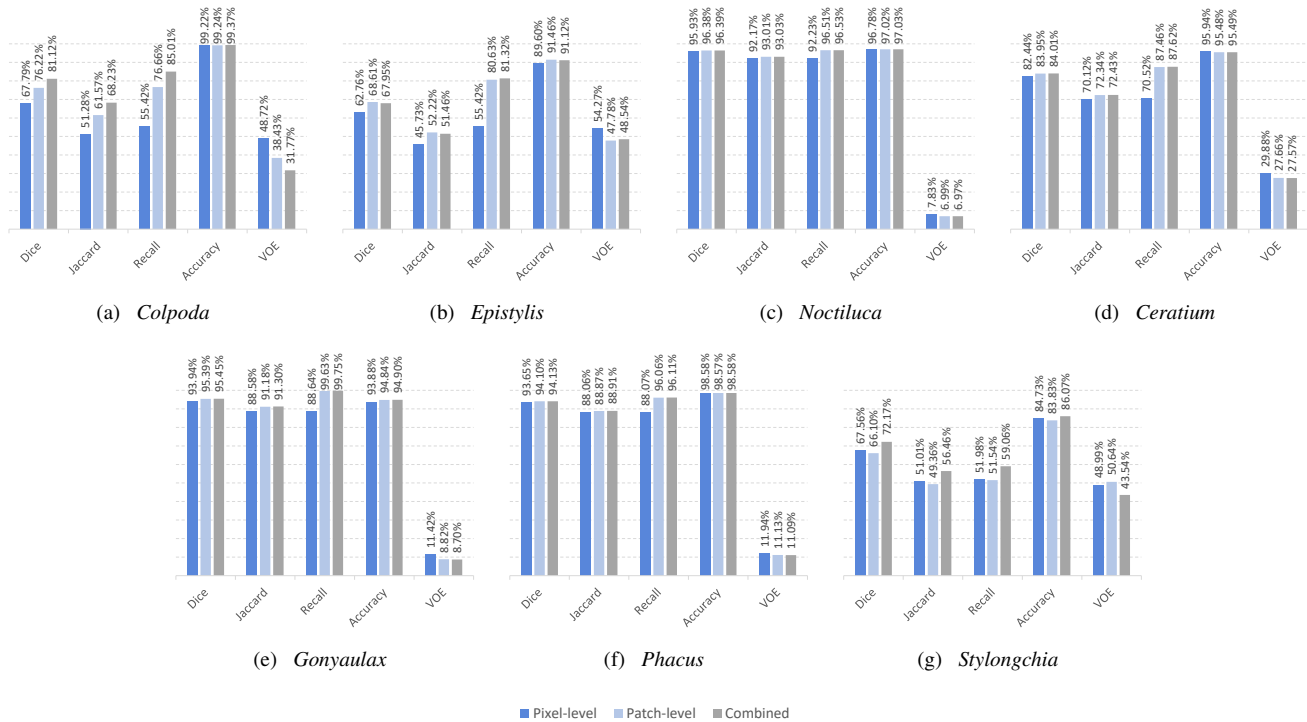


Fig. 24. The evaluation indexes for combined segmentation results.

Jaccard, Recall, Accuracy and VOE (volume overlap error) are 87.13%, 79.74%, 87.12%, 96.91% and 20.26%, respectively. Compared with U-Net, the first four indexes are improved by 1.89%, 2.32%, 4.84% and 0.14%, respectively, and the last index is decrease by 2.32%. In addition, compared with our previous methods in [3], the performance of segmentation results is significantly improved, and the details of indexes are shown in Fig. 19.

Owing to the fact that the method used in pixel-level segmentation cannot segment some details in the images, we want patch-level segmentation to render assistance to improve it. In the patch-level segmentation, we use transfer learning, which is using our data to fine-tune the pre-trained VGG16, to perform the patch-level segmentation task. We can find from Fig. 25 that the patch-level segmentation can effectively assist the pixel-level segmentation to cover more details.

In our future work, we plan to increase the amount of data in the data set in order to improve the performance. Meanwhile, we have not optimized the time requirement in pixel-level segmentation yet, but we will adjust the relevant parameters to reduce the time requirement.

VI. ACKNOWLEDGEMENTS

We thank Prof. Dr. Beihai Zhou, Dr. Fangshu Ma from the University of Science and Technology Beijing, PR China, Prof. Joanna Czajkowska from Silesian University of Technology, Poland and Prof. Yanling Zou from Freiburg university, Germany, for their previous cooperations in this work. We thank B.E. Xuemin Zhu from the Johns Hopkins University, US and B.E. Bolin Lu from Huazhong University of Science

and Technology, China, for their great work in the EMDS-5 ground truth image preparation. We also thank Miss Zixian Li and Mr. Guoxian Li, for their important discussion.

REFERENCES

- [1] R. Maier, I. Pepper, and C. Gerba, *Environmental Microbiology*. Academic Press, 2015.
- [2] C. Li, K. Shirahama, and M. Grzegorzec, "Application of Content-based Image Analysis to Environmental Microorganism Classification," *Biocybernetics and Biomedical Engineering*, vol. 35, no. 1, pp. 10–21, 2015.
- [3] S. Kosov, K. Shirahama, C. Li, and et al., "Environmental Microorganism Classification Using Conditional Random Fields and Deep Convolutional Neural Networks," *Pattern Recognition*, vol. 77, pp. 248–261, 2018.
- [4] C. Li, K. Wang, and N. Xu, "A Survey for the Applications of Content-based Microscopic Image Analysis in Microorganism Classification Domains," *Artificial Intelligence Review*, vol. 51, no. 4, pp. 577–646, 2019.
- [5] T. Yamaguchi, S. Kawakami, M. Hatamoto, and et al., "In Situ DNA-hybridization Chain Reaction (HCR): A Facilitated in Situ HCR System for the Detection of Environmental Microorganisms," *Environmental Microbiology*, vol. 17, pp. 2532–2541, 2015.
- [6] K. Simonyan and A. Zisserman, "Very Deep Convolutional Networks for Large-scale Image Recognition," 2014.
- [7] P. Krähenbühl and V. Koltun, "Efficient Inference in Fully Connected Crfs with Gaussian Edge Potentials," in *Proc. of NIPS 2011*, 2011, pp. 109–117.
- [8] C. Li, K. Shirahama, and M. Grzegorzec, "Environmental Microbiology Aided by Content-based Image Analysis," *Pattern Analysis and Applications*, vol. 19, no. 2, pp. 531–547, 2016.
- [9] F. Kulwa, C. Li, X. Zhao, and et al., "A State-of-the-art Survey for Microorganism Image Segmentation Methods and Future Potential," *IEEE Access*, vol. 7, pp. 100 243–100 269, 2019.
- [10] X. Yang, H. Beyenal, G. Harkin, and et al., "Evaluation of Biofilm Image Thresholding Methods," *Water Research*, vol. 35, no. 5, pp. 1149–1158, 2001.

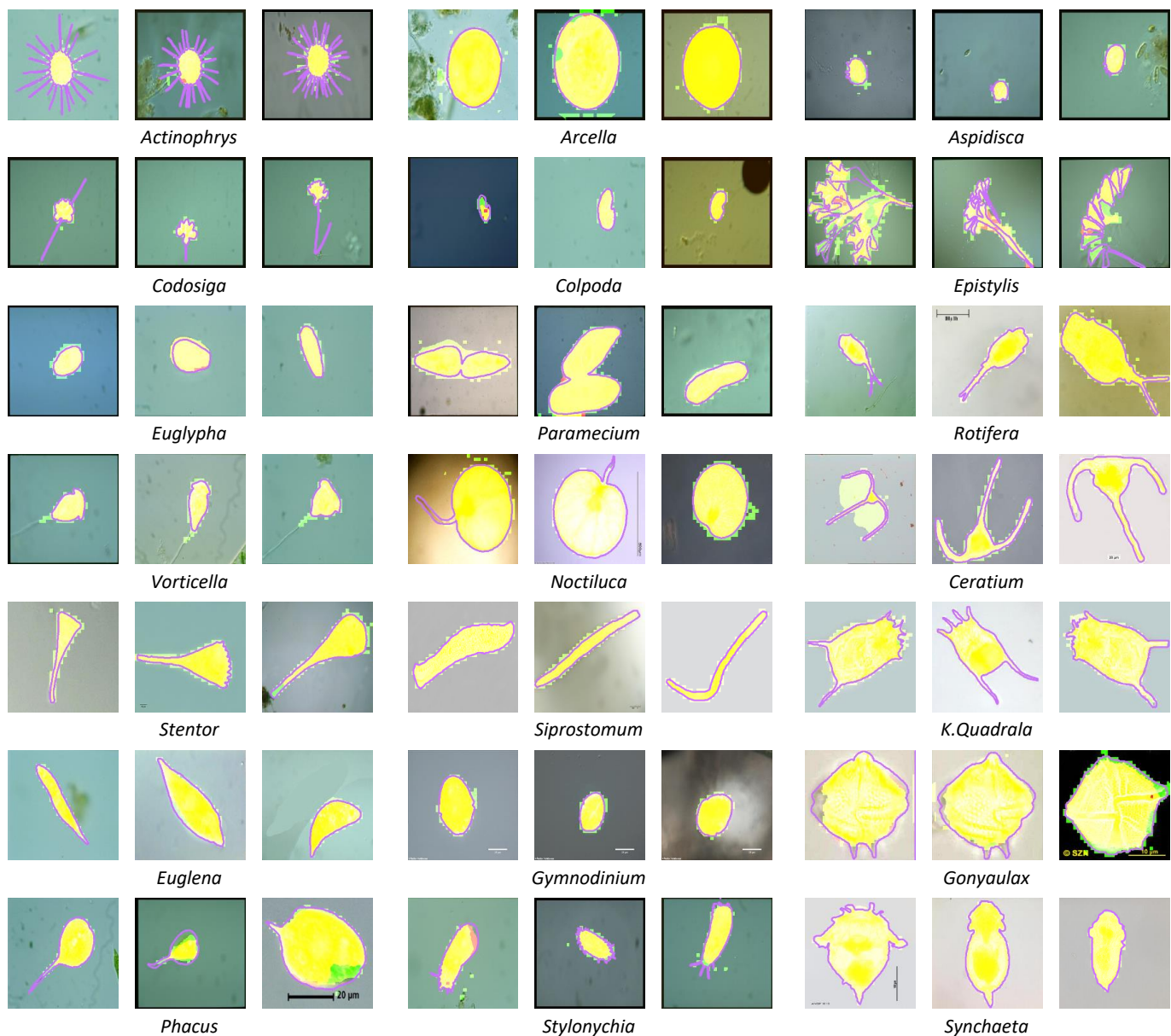


Fig. 25. The combined results of pixel-level segmentation results and patch-level segmentation results. The red and fluorescent green masks are pixel-level and patch-level segmentation results. The yellow masks represent the overlap of pixel-level and patch-level segmentation results. The purple outlines are the outlines of GT images.

- [11] M. Khan, H. Nisar, C. Ng, and et al., "Local Adaptive Approach Toward Segmentation of Microscopic Images of Activated Sludge Flocs," *Journal of Electronic Imaging*, vol. 24, no. 6, p. 061102, 2015.
- [12] M. Dubuisson, A. Jain, and M. Jain, "Segmentation and Classification of Bacterial Culture Images," *Journal of Microbiological Methods*, vol. 19, no. 4, pp. 279–295, 1994.
- [13] E. Gutzeit, C. Scheel, T. Dolereit, and et al., "Contour Based Split and Merge Segmentation and Pre-classification of Zooplankton in Very Large Images," in *Proc. of VISAPP 2014*, 2014, pp. 417–424.
- [14] P. Hiremath, P. Bannigidad, and M. Hiremath, "Automated Identification and Classification of Rotavirus-A Particles in Digital Microscopic Images," in *Proc. of RTIPPR 2010*, 2010, pp. 69–73.
- [15] M. Chayadevi and G. Raju, "Automated Colour Segmentation of Tuberculosis Bacteria Thru Region Growing: A Novel Approach," in *Proc. of ICADIWT 2014*, 2014, pp. 154–159.
- [16] M. Osman, M. Mashor, and H. Jaafar, "Performance Comparison of Clustering and Thresholding Algorithms for Tuberculosis Bacilli Segmentation," in *Proc. of CITS 2012*, 2012, pp. 1–5.
- [17] M. Kemmler, B. Fröhlich, E. Rodner, and et al., "Segmentation of Microorganism in Complex Environments," *Pattern Recognition and Image Analysis*, vol. 23, no. 4, pp. 512–517, 2013.
- [18] K. Dannemiller, K. Ahmadi, and E. Salari, "A New Method for the Segmentation of Algae Images Using Retinex and Support Vector Machine," in *Proc. of EIT 2015*, 2015, pp. 361–364.
- [19] D. Matuszewski and I. Sintorn, "Minimal Annotation Training for Segmentation of Microscopy Images," in *Proc. of ISBI 2018*, 2018, pp. 387–390.
- [20] O. Ronneberger, P. Fischer, and T. Brox, "U-Net: Convolutional Networks for Biomedical Image Segmentation," in *Proc. of MICCAI 2015*, 2015, pp. 234–241.
- [21] C. Szegedy, V. Vanhoucke, S. Ioffe, and et al., "Rethinking the Inception Architecture for Computer Vision," in *Proc. of CVPR 2016*, 2016, pp. 2818–2826.
- [22] C. Szegedy, W. Liu, Y. Jia, and et al., "Going Deeper with Convolutions," in *Proc. of CVPR 2015*, 2015, pp. 1–9.
- [23] L. Chen, G. Papandreou, I. Kokkinos, and et al., "Deeplab: Semantic Image Segmentation with Deep Convolutional Nets, Atrous Convolution, and Fully Connected Crfs," *IEEE Transactions on Pattern Analysis and*

- Machine Intelligence*, vol. 40, no. 4, pp. 834–848, 2017.
- [24] S. Zheng, S. Jayasumana, B. Romera-Paredes, and et al., “Conditional Random Fields as Recurrent Neural Networks,” in *Proc. of ICCV 2015*, 2015, pp. 1529–1537.
 - [25] Y. Cao, Z. Wu, and C. Shen, “Estimating Depth from Monocular Images as Classification Using Deep Fully Convolutional Residual Networks,” *IEEE Transactions on Circuits and Systems for Video Technology*, vol. 28, no. 11, pp. 3174–3182, 2017.
 - [26] N. Ibtehaz and M. Rahman, “MultiResUNet: Rethinking the U-Net Architecture for Multimodal Biomedical Image Segmentation,” 2019.
 - [27] S. Ioffe and C. Szegedy, “Batch Normalization: Accelerating Deep Network Training by Reducing Internal Covariate Shift,” 2015.
 - [28] J. Deng, W. Dong, R. Socher, and et al., “Imagenet: A Large-scale Hierarchical Image Database,” in *Proc. of CVPR 2009*, 2009, pp. 248–255.
 - [29] H. Shin, H. Roth, M. Gao, and et al., “Deep Convolutional Neural Networks for Computer-aided Detection: CNN Architectures, Aataset Characteristics and Transfer Learning,” *IEEE Transactions on Medical Imaging*, vol. 35, no. 5, pp. 1285–1298, 2016.
 - [30] Y. Zou, C. Li, K. Shirahama, and et al., “Environmental Microorganism Image Retrieval Using Multiple Colour Channels Fusion and Particle Swarm Optimisation,” in *Proc. of ICIP 2016*, 2016, pp. 2475–2479.
 - [31] F. Chollet and et al., “Keras,” 2015.
 - [32] M. Abadi, P. Barham, J. Chen, and et al., “Tensorflow: A System for Large-scale Machine Learning,” in *Proc. of OSDI 2016*, 2016, pp. 265–283.
 - [33] A. Taha and A. Hanbury, “Metrics for Evaluating 3D Medical Image Segmentation: Analysis, Selection, and Tool,” *BMC Medical Imaging*, vol. 15, no. 1, p. 29, 2015.